Hyperspectral Airborne "Viareggio 2013 Trial" Data Collection for Detection Algorithm Assessment

Nicola Acito, *Member, IEEE*, Stefania Matteoli, *Member, IEEE*, Alessandro Rossi, Marco Diani, *Member, IEEE*, and Giovanni Corsini, *Member, IEEE*

Abstract—For many years, the entire target detection scientific community has felt the urge for fully ground-truthed hyperspectral imagery data sets expressly released for testing and comparing detection algorithms. Although a few excellent data-sharing efforts have been carried out in the last decade, the use of either restricted or not well ground-truthed imagery still remains a common practice in the target detection literature. In this paper, we provide an overview of a new hyperspectral data set that we release to the scientific community with the specific goal of fostering unbiased comparison and scientific discussions of anomaly detection (AD), object detection, and anomalous change detection (ACD) algorithms. The data set is fully ground-truthed and documented and includes scenarios and experiments specifically conceived for detection algorithm comparison and benchmarking. Insights about the various possible data exploitation tasks are provided by making reference to noise estimation and reduction, AD, spectral signature-based target detection (SSBTD), and ACD. Experimental results concerning ACD and SSBTD are presented and highlight the usefulness of this new data set from the data sharing and algorithmic comparison perspectives.

Index Terms—Anomalous change detection (ACD), anomaly detection (AD), free hyperspectral imagery, spectral signatures, target detection.

I. INTRODUCTION

THE development and testing of advanced processing algorithms capable of going beyond the state-of-the-art in various hyperspectral remote sensing applications demand for the availability of well ground-truthed hyperspectral imagery data sets freely accessible to the scientific community. This has been recognized as a fundamental requirement to enable unbiased algorithm comparison as well as scientific debate [18], [22], [32].

The need of available hyperspectral ground-truthed data sets has been promptly and continuously responded by the land-cover classification community [2]—starting from the very well-known "Indian Pine" data set, distributed in the early nineties by Purdue University [1], up to the "Pavia" data set,

acquired in the framework of the HySenS project managed by DLR and sponsored by EU. However, no such similar commitment has been demonstrated by the target-detection community until the very last decade, when the lack of available well ground-truthed imagery for detection applications has been recognized as one of the major challenges for the hyperspectral target detection research community [32], [18]. Until then, several research groups have collected, ground-truthed, and analyzed their own data by restricting their distribution mostly due to the cost associated with data collection and ground-truthing as well as to security issues [12], [14], [15], [19], [21], [24], [33]. Other researchers have implanted synthetic targets into nonground-truthed available images [10], [11]. In other cases, researchers have employed data with an uncertain ground truth or lacking a statistically significant number of background pixels sufficient to assure reliable performance evaluation.

Following the recommendation in [18] and [32], the major efforts toward fully ground-truthed data-sharing came from one single research group, i.e., the DIRS group of the Rochester Institute of Technology. Specifically, the DIRS group released the "Cooke City" [32], SHARE 2010 [16], and SHARE 2012 [13] data sets in 2008, 2012, and 2013, respectively. These data include several hyperspectral images acquired over one or more scenarios featuring targets with accurate ground truth. In some cases, data acquired from sensors other than hyperspectral are also included. The main characteristics of the data sets, with specific attention to hyperspectral imagery, are summarized in Table I.

Although these data sets have been employed by many researchers around the world, the use of either restricted or not well documented imagery still remains a common practice. More importantly, as very well expressed by the words of Manolakis, in order to reliably validate and compare detection algorithms without the risk of obtaining anecdotal results one would "*need well-truthed data sets for a diverse range of targets and backgrounds under various scenarios, target fill-factors, and atmospheric conditions*" [20]. Therefore, there is still need for new data sets to be made accessible to the target detection community.

The goal of this paper is to introduce and describe a new data set that we release to the target detection community following the way paved by the aforementioned data-sharing efforts [13], [16], [32]. This data set is not intended to replace any of the existing shared data sets. Rather, it is provided in order to enrich the arena of detection algorithm comparison with data acquired from a different sensor and featuring different scenarios, materials, objects, and conditions.

TABLE I
MAIN CHARACTERISTICS OF THE DATA SETS AVAILABLE TO THE TARGET
DETECTION SCIENTIFIC COMMUNITY, WITH SPECIFIC ATTENTION TO
HYPERSPECTRAL IMAGERY

DATA SET	'Cooke City'	SHARE 2010	SHARE 2012
Scenario	Rural	Urban/rural/water	Suburban/rural
Hyperspectral Sensor	HyMap	ProSpecTIR-VS2	ProSpecTIR-VS2
Elevation AGL (Km)	~1.55	~0.77/1.52/2.29	~1.50/2.50
IFOV (mrad)	2.0/2.5 across/along track	1.3	1.3
Spectral range (nm)	454 − 2496	390 − 2450	400 − 2450
# channels	126	360	360
Average FWHM (nm)	~16	~5	~5
Other sensors	✗	✓	✓
Multi-temporal	✓	✓	✓
Radiance imagery	✓	✓	✓
Reflectance imagery	✓	✓	✓
Ground truth	✓	✓	✓
Target ROIs	✓	✗	✗
Performance evaluation system	✓	✗	✗
Reference	[32]	[16]	[13]
Research group	DIRS	DIRS	DIRS

During the data collection campaign, *ad hoc* scenarios and experiments were set up with the specific goal of enabling the test of anomaly detection (AD), anomalous change detection (ACD), and spectral signature-based target detection (SSBTD) algorithms. A selection of fully ground-truthed imagery is released to the scientific community by means of a website for easy-to-access extensive documentation and data download.

This paper is organized as follows. Section II describes the data collection campaign as well as sensors and instrumentation employed. The specific data released for sharing purpose are illustrated in detail in Section III, which focuses on acquired scenarios, shared imagery, ground truth, and data preprocessing. Section IV presents an overview about possible ways of shared data exploitation, with particular attention to the ACD and SSBTD tasks. Finally, Section V summarizes the main contributions of the work.

II. "VIAREGGIO 2013 TRIAL" HYPERSPECTRAL DATA COLLECTION

The "Viareggio 2013 trial" hyperspectral data collection campaign was organized by CISAM (Centro Interforze Studi e Applicazioni Militari) with the support of CSSN-ITE (Centro Supporto Sperimentazioni Navali—Istituto per le Telecomunicazioni e l'Elettronica), Selex ES, and University of Pisa [27]. The campaign was held in Viareggio (Italy), in May 8 and 9, 2013. The city of Viareggio offered the possibility of including different types of scenarios, ranging from rural, through beach (desert-like) and water, to suburban and urban scenarios.

Fig. 1. Sketch of the four land scenarios, with highlighted hyperspectral sensor swaths (red: VNIR swath at 1200 m; yellow: SWIR swath at 450 m). For each scenario, an RGB image extracted from the collected hyperspectral imagery is shown.

TABLE II
BRIEF DESCRIPTION OF SCENARIOS

SCENARIO	α	β	γ	δ
LOCATION	Parking lot in suburban vegetated area	Parking lot, street, public garden	Beach, sand dunes, Mediterranean vegetation, water	Urban downtown area
TARGETS	Vehicles, panels, tarps — calibration tarps	Vehicles, panels, tarps	Array of panels, clothing targets	Vehicles
MULTITEMPORAL ACTIVITY	Several targets changed location within α scenario and moving to/from β scenario	Several targets changed location within β scenario and moving to/from α scenario	Several targets changed location within γ scenario	Two targets moved from δ scenario to scenarios α and β

A. Data Collection Campaign

An ultralight aircraft flew over the Viareggio area at different times and at two different elevations, i.e., about 1200 and 450 m. These two elevations were selected in order to provide data in the visible near infrared (VNIR) and short-wave infrared (SWIR) with the same ground spatial resolution.

Some scenarios were set up in collaboration with the Italian Navy in the water [27] and are not examined here. Rather, we focus on the four land scenarios of different complexities depicted in Fig. 1 and summarized in Table II. Vehicles, panels, tarps, and different man-made objects served as targets and were deployed across the four scenarios in parking lots, rural vegetation areas, beach, and Viareggio downtown. Some of the targets were moved from one location to another (both within the same scenario and across two scenarios) in-between two subsequent flights and across the two days.

Accurate ground truth of all scenarios and target configurations was carried out during each flight. The selected personnel monitored and recorded any changes occurring in the areas where the targets were deployed. The presence of "targets of opportunity," such as other vehicles in the urban scenarios or man-made materials deployed on the beach or in suburban areas was carefully documented.

In Section III, a more detailed description is provided focusing on the subset of data that has been selected for sharing purposes.

TABLE III
SIM.GA SENSOR CHARACTERISTICS

CHARACTERISTICS	SIM.GA VNIR	SIM.GA SWIR
Imagine	Pushbroom	
Spectral range (nm)	400 – 1000	1000 – 2500
Spectral sampling (nm)	≈ 1.2	≈ 5.8
# Spectral bands	512	256
# Spatial pixels	1024	320
Nominal IFOV (mrad)	0.499	1.330
Field of view (FOV) (°)	± 15	± 12

TABLE IV
PAN CAMERA CHARACTERISTICS

CHARACTERISTICS	PAN
Spectral range (nm)	450 –900
Spatial pixels	4096
IFOV (mrad)	0.134
Field of view (FOV) (°)	31.36
Focal length (mm)	50
Digital resolution (bit)	8
Operating frame rate (Hz)	1000

TABLE V
FIELDSPEC SPECTRORADIOMETER CHARACTERISTICS

CHARACTERISTICS	FIELDSPEC ® Pro FR
Spectral range (nm)	350 – 2500
Spectral resolution (nm)	3 at 700 nm 10 at 1400 nm & 2100 nm
Sampling interval (nm)	1.4 at 350 – 1050 nm 2 at 1000 – 2500 nm
Scanning time (nm)	100

B. Instrumentation

During the collection campaign, two airborne sensors were used: 1) the pushbroom hyperspectral SIM.GA sensor and 2) a panchromatic (PAN) camera. Furthermore, the FieldSpec spectroradiometer and a differential GPS were employed at ground during ground-truthing operations.

1) Airborne Instrumentation: SIM.GA is an avionic hyperspectral instrument manufactured by Selex ES. The electro-optical head is equipped with two sensors (operating in the VNIR and SWIR ranges) and the instrument control unit/preprocessing computer manages the optical head and performs internal data storage. The characteristics of SIM.GA sensor are reported in Table III. The ground spatial resolution at 1200 m is about 0.6 and 1.6 m in the VNIR and SWIR, respectively. When flying at 450 m, SWIR ground spatial resolution is about 0.6 m.

SIM.GA instrument is the result of several years of research and experiments by Selex ES with various scientific communities and will be replaced by a new product, i.e., SPHYDER, which will be launched in 2016. This off-the-shelf product has the capability of providing real-time results of the acquired and processed data. The results of the data processing have remarkably improved with SPHYDER instrument thanks to the enhanced spatial resolution and the on-board calibration hardware that extend the range of the operating conditions.

The PAN camera was employed so as to collect higher spatial resolution imagery of the monitored area. Its main characteristics are listed in Table IV.

2) Ground Instrumentation: In order to collect measures of direct and downwelled spectral irradiance as well as of spectral reflectance of the various targets and reference calibration tarps, the FieldSpec hand-held spectroradiometer was employed at ground. Its main specifics are summarized in Table V. Such measurements are necessary to apply atmospheric compensation/forward modeling techniques both model-based (e.g., MODTRAN-based [9], [23]) and image-based [e.g., empirical line method (ELM) [31]], and to run SSBTD algorithms.

During ground-truthing operations, all target locations were accurately recorded by means of the differential GPS Leica
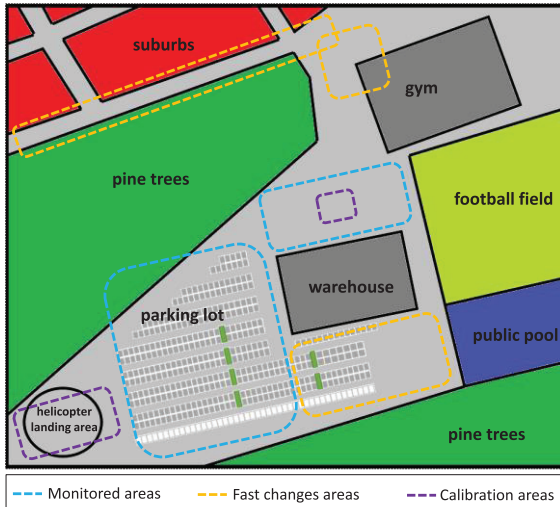
1200, which is a dual-frequency geodetic receiver enabling a measurement accuracy of approximately 2 cm.

III. "VIAREGGIO 2013 TRIAL" SHARED DATA DESCRIPTION

Of the entire amount of imagery collected during the "Viareggio 2013 trial," a subset of three images acquired over the α scenario (Fig. 1) has been so far selected for sharing purposes. The α scenario was chosen because, besides targets, it also includes white and black reference calibration tarps spectrally characterized on the field by means of the FieldSpec. The presence of these tarps may be useful to carry out image-based atmospheric compensation algorithms such as the ELM [31]. In the future, additional images acquired over different scenarios may be released for sharing purpose, thus further enriching the hyperspectral data archive available to the scientific community.

A. Scenario Description

The selected images include a parking lot, where most of the targets were deployed, several sports facility buildings, and a football field. The parking lot is surrounded by small groves with pine trees and some clearings and the north grove adjoins a residential suburban area. A pictorial representation of the scenario is depicted in Fig. 2. The targets of interest were deployed within the light blue boxes in the figure. During the acquisitions, these areas were not very crowded and, thus, all other vehicles and objects besides the deployed targets were accurately monitored and documented by the assigned personnel.

Fig. 2. Pictorial representation of α scenario.

TABLE VI
SHARED IMAGERY CHARACTERISTICS

CHARACTERISTICS	D1F12H1	D1F12H2	D2F22H2
DAY	May 8, 2013	May 8, 2013	May 9, 2013
Time (GMT)	14.18	14.33	12.64
Elevation AGL (Km)	1.24		
LATITUDE	43° 51′ 25″ N		
Longitude	10° 14′ 51″ E		
Sky conditions	cloud cover	cloud cover	clear
Scenario	α		
Samples	450		
Lines	375		
Bands	511		
Spectral range	VNIR		
Radiance units	$W \cdot m^{-2} \cdot sr^{-1} \cdot \mu m^{-1}$		

The yellow boxes in the figure highlight the "fast changes" areas, which mostly refer to a road and a crowded portion of the parking lot. During and across the acquisitions, many movements and changes occurred within these areas and they were accurately recorded. The purple boxes in the figure make reference to the calibration areas, where the white and black reference calibration tarps were deployed.

B. Shared Imagery and Corresponding Ground Truth

Three images acquired by the VNIR camera of the SIM.GA sensor flying at 1200 m were selected. The main characteristics of these images are listed in Table VI. D1F12H1 and D1F12H2 images were acquired on May 8, when the sky was characterized by a thick cloud cover and the main source of illumination was downwelled irradiance scattered from the sky. D2F22H2 image was acquired the following day in clear
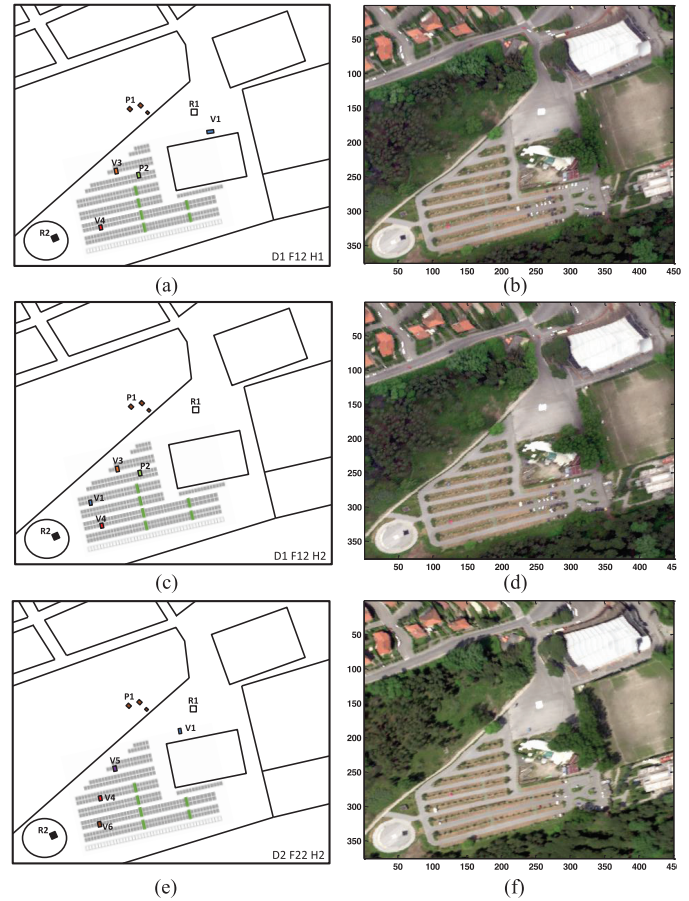

Fig. 3. (a, c, e) Sketches with target locations and (b, d, f) corresponding RGB representations of the three images. (a, b) D1F12H2; (c, d) D1F12H2; (e, f) D2F22H2.

sky and high-visibility conditions. Here, the presence of a strong direct solar irradiance component determined shadows in the image that may be particularly useful for testing shadow removal algorithms.

Sketches of deployed target locations within the three images along with corresponding RGB representations are shown in Fig. 3 (a)–(f). A description of the deployed targets, together with reference calibration tarps, can be found in Table VII, whereas the corresponding photos are depicted in Fig. 4. Fig. 5 shows the reflectance spectra of targets and calibration tarps as acquired by the FieldSpec. Table VIII shows which of the deployed targets is present in each of the distributed images.

Ground truth data are released on the website in form of both ASCII and ENVI files as regards 1) location and 2) spectral reflectance of targets and calibration tarps as well as 3) change reference maps (CRMs). The CRMs include all recorded changes occurred in the scene across the various acquisitions. For a given pair of images, two CRMs are provided where the two images are assumed in turn as "reference" and "test" images. Each CRM denotes the "insertion" changes involving those objects that are not present in the "reference" image but appear in the "test" image. The CRMs are provided for the "D1F12H1–D1F12H2" and "D1F12H1–D2F22H2" image pairs, which span an in-between acquisition time interval of 15 minutes and nearly one day (about 22 h), respectively. Fig. 6

TABLE VII
DESCRIPTION OF TARGETS AND REFERENCE CALIBRATION TARPS

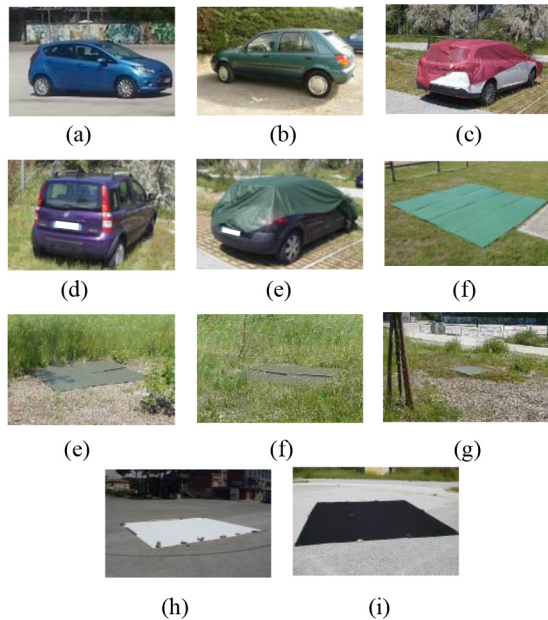| TARGET		DESCRIPTION
V1		Blue vehicle
V3		Green vehicle
V4		White vehicle covered with red tarp
V5		Purple vehicle
V6		Black vehicle covered with green tarp
P1	P1_1	Green panel
	P1_2	Green panel
	P1_3	Green panel
P2		Bright green panel
R1		White reference calibration tarp
R2		Black reference calibration tarp

Fig. 4. Photos of the deployed targets and reference calibration tarps. (a) V1; (b) V3, (c) V4; (d) V5; (e) V6; (f) P2; (e) P1_1; (f) P1_2; (g) P1_3; (h) R1; (i) R2.

shows the CRMs for each of the shared image pair, super-imposed to the RGB representation of the corresponding test image.

Table IX shows the number of changed objects in each CRM.

C. Data Preprocessing

Prior sharing, the data were preprocessed in order to improve image quality. First, the residual striping noise was removed by resorting to a multilinear regression approach that also accounts for signal dependencies [4]. Then, noise parameters were estimated with the HYNPE algorithm [3] and the signal dependent noise variance was estimated on a per-pixel basis.
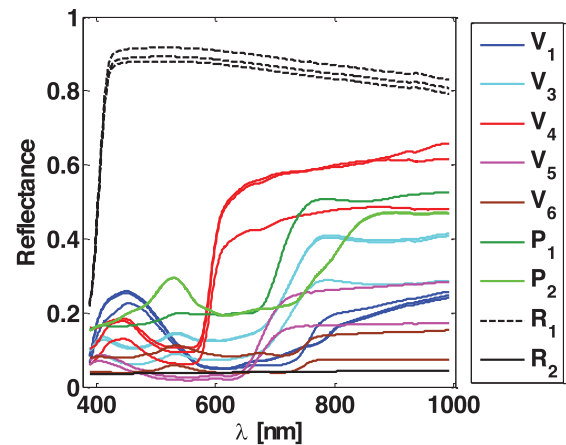

Fig. 5. Reflectance spectra of targets and reference calibration tarps.

TABLE VIII
TARGETS PRESENT IN EACH SHARED IMAGE

TARGET		D1F12H1	D1F12H2	D2F22H2
V1		✓	✓	✓
V3		✓	✓	✗
V4		✓	✓	✓
V5		✗	✗	✓
V6		✗	✗	✓
P1	P1_1	✓	✓	✓
	P1_2	✓	✓	✓
	P1_3	✓	✓	✓
P2		✓	✓	✗
R1		✓	✓	✓
R2		✓	✓	✓

Such estimates were used to normalize the noise variance in each band and for each pixel (noise-whitening). A spectral binning was also performed, by averaging the data over groups of four consecutive spectral channels (i.e., binning factor, $BF = 4$). After preprocessing, a spatial subset was extracted from the larger original image associated with D1F12H1. The same spatial subset was extracted from the associated input geometry (IGM) file, thus allowing for co-registration of the other two images over D1HF12H1.

A sketch of the preprocessing flow is shown in Fig. 7. The data are released on the website with five different preprocessing levels: 1) original data (for D1F12H1 only); 2) de-striped data; 3) de-striped and spectrally binned data; 4) de-striped and noise-whitened data; and 5) de-striped, noise-whitened, and spectrally binned data.

D. Website for Data Sharing

The data described in the previous sections are available online at http://rsipg.dii.unipi.it/. The data can be accessed and downloaded for free upon registration to the website.
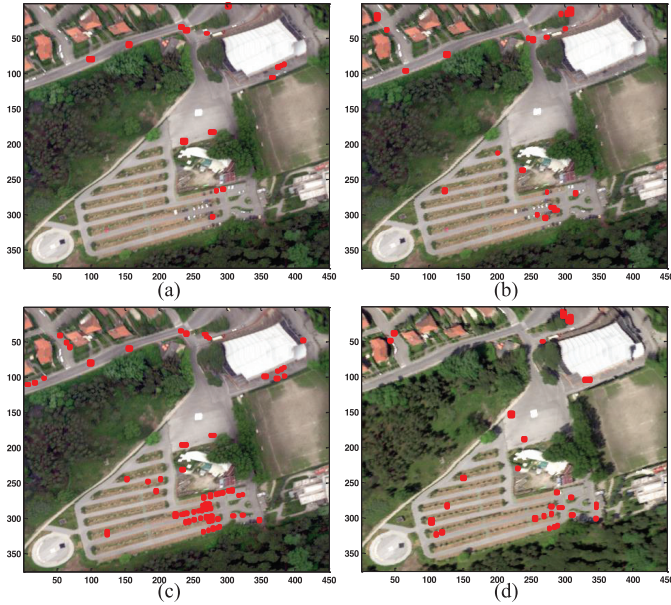
Fig. 6. CRMs between image pairs. Insertion changes from "reference" to "test" image are shown in red. (a, b) "D1F12H1–D1F12H2" image pair; (c, d) "D1F12H1–D2F22H2" image pair. (a) D1F12H2 is "reference" image and D1F12H1 is "test" image; (b) D1F12H1 is "reference" image and D1F12H2 is "test" image; (c) D2F22H2 is "reference" image and D1F12H1 is "test" image; (d) D1F12H1 is "reference" image and D2F22H2 is "test" image.

TABLE IX
NUMBER OF CHANGED OBJECTS IN EACH CRM

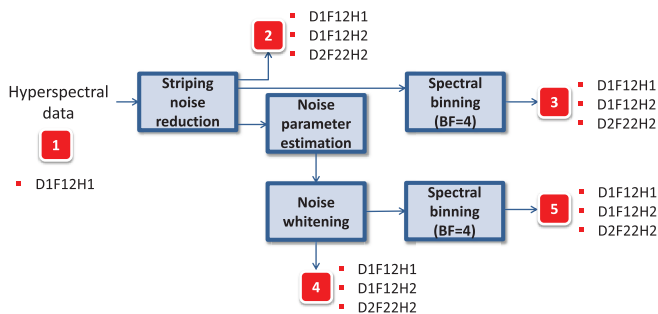| CHANGE REFERENCE MAP (REFERENCE−TEST)	NUMBER OF RECORDER CHANGES
D1F12H1–D1F12H2	21
D1F12H2–D1F12H1	15
D2F22H2–D1F12H1	66
D1F12H1–D2F22H2	29

Fig. 7. Data preprocessing flowchart. Red boxes indicate the different preprocessing levels of the released data.

Fig. 8 shows a screenshot of the website home page.

In addition to the data download section, the website contains a brief description of the measurement campaign and detailed information about shared data file organization.

IV. SHARED DATA EXPLOITATION

The shared data containing both hyperspectral images and ground-truth data represent a valuable tool for testing and

Fig. 8. Home page of the website (http://rsipg.dii.unipi.it/).

comparing different hyperspectral image processing tasks including noise estimation and reduction, AD, SSBTD, and ACD.

In this section, we first take a look at the potential use of the shared data and then explore in more detail their usefulness with reference to SSBTD and ACD applications by presenting and discussing some experimental results.

As concerns noise estimation and reduction, the shared data include a raw version (i.e., not preprocessed) of the D1F12H1 image that is affected by residual striping noise. This makes such an image suitable to test algorithms aimed at reducing this specific fixed pattern noise component. Furthermore, the raw version of D1F12H1 image is also affected by signal-dependent noise (due to photon noise). As confirmed by several recently published papers [3], [25], [36], there has been growing interest in the hyperspectral scientific community toward this signal dependent random noise contribution because it cannot be neglected in data collected by new-generation sensors. Thus, the raw version of D1F12H1 image can be considered as a sort of test bed for comparing and validating algorithms aimed at characterizing the random noise in the presence of a signal dependent component.

The availability of several different ground-truthed targets in the three images can be exploited for testing AD algorithms in terms of their capability in suppressing the background pixels while emphasizing the pixels containing the known targets. Furthermore, as shown in a recent work [6], some AD algorithms might benefit from normalization of the data with respect to noise variance—specifically in case of data affected by signal dependent noise. For each of the three shared images, the data set includes both the original noisy image and the noise-normalized one (whitened). This can be exploited to investigate the impact of noise normalization on the results provided by different AD algorithms and to extend the conclusions drawn in [6] for the RX algorithm.

The shared data may also be employed for testing and comparing SSBTD algorithms. In fact, knowledge of the exact location of the various targets in the scenes can be exploited to analyze the results provided by those algorithms that search the image for the targets by making use of the target spectral signature. Specifically, two kinds of experiments may be carried out. In the first experiment, the radiance spectrum extracted in correspondence of the location of a given target in one image may be assumed as known target spectral signature and exploited to search that given target in another image. This can be performed by considering D1F12H1 and D1F12H2 images, which were collected with a time delay of few minutes and therefore, under very similar acquisition conditions. Furthermore, the two corresponding scenes contain the same set of controlled targets. The interest in performing such experiment is testing SSBTD algorithms by just focusing on the detection step, without including uncertainty due to the transformation from radiance to reflectance domain. Because the shared data are equipped with a reflectance spectral library of target spectral signatures, the data also enable testing SSBTD algorithms in the more realistic case when the target of interest is spectrally characterized in the reflectance domain. For this purpose, the available reflectance spectra of the white and the black calibration tarps along with the knowledge of the exact positions of such tarps in each image can be exploited to estimate the transformation from radiance to reflectance domain (for instance, by resorting to the ELM). Then, the measured reflectance spectra of each target can be used to search for the presence of that target in the transformed image. It is worth noting that, in the case of SSBTD algorithms, a quantitative analysis of the detection performance for comparison purposes can be carried out by resorting to specific performance indexes such as the false alarm rate at first Detection (FAR@1stD) [22]. An example of SSBTD algorithms application will be provided in the next section.

Finally, the multitemporal nature of the shared data makes them particularly suitable for testing and comparing ACD algorithms. A detailed example of shared data exploitation as specifically regards the ACD task is provided in the following section, where emphasis is placed on the usefulness of the shared data set for testing and comparing various algorithms both in terms of overall performance and by restricting the analysis to each step of the ACD processing chain.

A. SSBTD: Comparison of Three Different Algorithms

In this section, we show how the data can be used to compare the performance of different SSBTD algorithms. For this purpose, we consider the three at sensor radiance images and the targets described in Table VII. In order to apply a given SSBTD algorithm, the image data and the known target spectral signature must be made radiometrically comparable. This means that a given transformation from the reflectance to the radiance domain has to be adopted. The available reflectance spectra of the white and the black calibration tarps along with the knowledge of their exact location in each image allow the transformation to be estimated by resorting to the ELM.

Once the reflectance spectra of the targets have been transformed in the radiance domain, a specific SSBTD algorithm can be applied with the aim of searching the targets in a given image. In this section, we consider three *state-of-the-art* SSBTD algorithms known as the adaptive cosine estimator (ACE) [38], the Kelly detector (Kelly) [37], and the subspace-based generalized likelihood ratio test (SBGLRT) [33]. Since we have more than one spectral signature for the most of the ground-truthed targets, the subspace-based versions of the ACE and Kelly detector are used. For each target, we consider as target subspace the one addressed by the available spectral signatures after the transformation in the radiance domain. The three algorithms rely on a threshold based decision rule, where a decision statistic obtained from the data is compared with a threshold in order to decide for the presence of the target in the image. The detection statistics for the three considered algorithms are reported as follows:

$$T_{ACE}(\mathbf{x}) = \frac{\mathbf{x}^T \cdot \mathbf{C}^{-1} \cdot \mathbf{S} \cdot \left(\mathbf{S}^T \cdot \mathbf{C}^{-1} \cdot \mathbf{S}\right)^{-1} \cdot \mathbf{S}^T \cdot \mathbf{C}^{-1} \cdot \mathbf{x}}{\mathbf{x}^T \cdot \mathbf{C}^{-1} \cdot \mathbf{x}}$$

(1)

$$T_{KELLY}(\mathbf{x}) = \frac{\mathbf{x}^T \cdot \mathbf{C}^{-1} \cdot \mathbf{S} \cdot \left(\mathbf{S}^T \cdot \mathbf{C}^{-1} \cdot \mathbf{S}\right)^{-1} \cdot \mathbf{S}^T \cdot \mathbf{C}^{-1} \cdot \mathbf{x}}{1 + \frac{1}{N}\mathbf{x}^T \cdot \mathbf{C}^{-1} \cdot \mathbf{x}}$$

(2)

$$T_{SBGLRT}(\mathbf{x}) = \frac{\mathbf{x}^T \cdot \mathbf{P}_{\mathbf{B}}^{\perp} \cdot \mathbf{x}}{\mathbf{x}^T \cdot \mathbf{P}_{\mathbf{BS}}^{\perp} \cdot \mathbf{x}}$$

(3)

where $\mathbf{x}$ represents the generic image pixel, $\mathbf{C}$ is the estimate of the background covariance matrix obtained from a set of N secondary data, $\mathbf{S}$ is the basis matrix for the target subspace, $\mathbf{P}_{\mathbf{B}}^{\perp}$ is the projection matrix on the orthogonal complement of the background subspace, and $\mathbf{P}_{\mathbf{BS}}^{\perp}$ is the projection matrix on the subspace orthogonal to both the background and the target.

In the proposed experiments, the background covariance matrix for both the ACE and the Kelly detector is estimated in a global fashion by using all the image pixels. Thus, the number N of the auxiliary data equals the number of the image pixels. Furthermore, the background subspace basis matrix for the evaluation of $\mathbf{P}_{\mathbf{B}}^{\perp}$ and $\mathbf{P}_{\mathbf{BS}}^{\perp}$ in the SBGLRT detector is estimated by resorting to the Hysime algorithm [39].

In order to assess the performance of each SSBTD algorithm, the FAR@1stD has been evaluated for each ground-truthed target. The FAR@1stD for a given target is obtained by computing the fraction of the image pixels included in the background region (outside the target reference map) whose detection statistic assumes values higher than a certain threshold λ. Here, the threshold is the maximum value of the detection statistic in the region of the image occupied by the considered target. Thus, FAR@1stD denotes the FAR in the image when at least one of the pixels of the target of interest is detected.

Tables X–XII show the FAR@1stD and the corresponding number of false alarm pixels obtained by applying the three SSBTD algorithms to each target in the three shared images. In this example, we used the binned data after striping reduction.

Tables X–XII are an example of how the shared data can be used for algorithm performance ranking with reference to the specific scenario acquired during the measurement campaign.

Results show that in all the proposed experiments, the best performing algorithm is the ACE. Particularly, it is important

TABLE X

IMAGE D1F12H1: FAR@1stD AND NUMBER OF FALSE ALARM PIXELS AT THE FIRST DETECTION FOR EACH DEPLOYED TARGET

	D1F12H1					
	ACE		KELLY		SBGLRT	
TARGET	FAR@1stDET	#FA pixels	FAR@1stDET	#FA pixels	FAR@1stDET	#FA pixels
V4	0	0	0	0	0	0
V3	5,93E-06	1	1,13E-04	19	1,01E-04	17
V1	1,07E-04	18	1,24E-04	21	5,93E-06	1
P2	0	0	5,93E-05	10	5,93E-06	1
P1_1	0	0	5,33E-05	9	0	0
P1_2	0	0	1,30E-04	22	0	0
P1_3	0	0	3,56E-04	60	1,54E-04	26

TABLE XI

IMAGE D1F12H2: FAR@1stD AND NUMBER OF FALSE ALARM PIXELS AT THE FIRST DETECTION FOR EACH DEPLOYED TARGET

	D1F12H2					
	ACE		KELLY		SBGLRT	
TARGET	FAR@1stDET	#FA pixels	FAR@1stDET	#FA pixels	FAR@1stDET	#FA pixels
V4	0	0	0	0	0	0
V3	5,9268E-06	1	1,42E-04	24	0	0
V1	5,92663E-06	1	2,37E-05	4	4,03E-04	68
P2	0	0	3,56E-05	6	0	0
P1_1	0	0	9,48E-05	16	0	0
P1_2	0	0	1,60E-04	27	0	0
P1_3	0	0	3,02E-04	51	2,07E-04	35

TABLE XII

IMAGE D2F22H2: FAR@1stD AND NUMBER OF FALSE ALARM PIXELS AT THE FIRST DETECTION FOR EACH DEPLOYED TARGET

	D2F22H2					
	ACE		KELLY		SBGLRT	
TARGET	FAR@1stDET	#FA pixels	FAR@1stDET	#FA pixels	FAR@1stDET	#FA pixels
V4	0	0	0	0	0	0
V1	4,15E-05	7	5,93E-05	10	5,93E-06	1
P1_1	0	0	3,56E-05	6	1,19E-05	2
P1_2	1,19E-05	2	1,31E-03	221	1,85E-03	312
P1_3	1,19E-05	2	9,84E-04	166	1,07E-01	17994
V5	0	0	2,37E-05	4	0	0
V6	0	0	2,02E-04	34	2,37E-04	40

to notice that the ACE outperforms the other two algorithms in detecting the panel named P1_3 that is a subpixel target. ACE detects the subpixel target with zero false alarms in both the images acquired during the first day. Its performance slightly degrades in the D2F22H2 image (two false alarm pixels) which was acquired under cloudy sky condition and is characterized by a lower signal to noise ratio. Notice that, as expected, all the considered algorithms have the worst performance in the image with the lowest signal to noise ratio.

B. ACD Example Results

1) ACD Basics: Change detection (CD) can be performed over two multitemporal hyperspectral data. Broadly speaking, a CD algorithm takes two images (generally called the "reference" image and the "test" image) as inputs and generates a single image as output, the so-called "change statistic." The pixels with the highest values in the change statistic should be associated with the relevant changes occurred in the temporal dimension. Here we make reference to a specific kind of CD,

i.e., the anomalous CD (ACD) [26], [28], [29], [30], [34], which aims at detecting small changes resulting from insertion, deletion, or movement of small-sized (and generally man-made) objects, as well as from small stationary objects whose spectrum changes from one image to another, as in the case of camouflage, concealment, and deception. ACD finds its major application in airborne surveillance and monitoring [34], [26].

Two main problems have to be tackled in ACD. The first is related to geometrical coregistration of "test" and "reference" images. Especially in airborne applications, perfect registration of the images is very difficult to achieve because of the unavoidable onboard instrumentation errors. Thus, a residual misregistration error (RMRE) inevitably remains. The RMRE has been shown to reduce the detection performance of pixel-based ACD algorithms [17]. In order to mitigate the detrimental effects of RMRE, the local coregistration adjustment (LCRA) [35] approach can be adopted. Such an approach consists in comparing the tested pixel of the "test" image with the pixels belonging to a neighborhood of the corresponding pixel in the "reference" image. The neighborhood is defined by an uncertainty window (UW) whose size is chosen in accordance with the magnitude of the RMRE [35].

The second problem arising in ACD applications is mostly due to physical constraints associated with the acquisition process. The energy collected by the sensor at a given acquisition time does not coincide with the energy emitted or reflected from the same portion of the scene observed at a different time. This is mainly due to variations occurred in atmospheric conditions, Sun azimuth and elevation angles, aerosols, and illumination conditions. Therefore, in order to make multitemporal images *radiometrically comparable*, these radiometric distortions should be corrected by means of a radiometric equalization (RE) process. RE may be accomplished by transforming the at-sensor radiance images in the reflectance domain or, more easily, by applying image-based RE transformations such as the ChronoChrome (CC) [30] and the covariance equalization (CE) [29].

In summary, the generic ACD processing chain is composed of three steps: 1) RMRE mitigation; 2) RE; and 3) application of the change decision strategy.

2) Experimental Description: In the following, two examples are presented where ACD is accomplished considering two couples of images extracted from the shared data. The examples show how the hyperspectral images and the related ground truth can be exploited to compare different ACD schemes and to analyze the single steps of the ACD processing chain. In the first example (EX-1), we consider D1F12H1 and D1F12H2 images, which were acquired on the same day and with very similar illumination and atmospheric conditions. Particularly, D1F12H1 is assumed to be the "test" image and D1F12H2 is taken as "reference" image. The CRM showing the objects that are not present in the "reference" image but appear in the "test" image is displayed in Fig. 6(a). In the second example (EX-2), the changes that appear in D1F12H1 ("test" image) when it is compared with D2F22H2 ("reference" image) are sought. This exemplifies the case of images collected in different days and under different acquisition conditions. The CRM for the
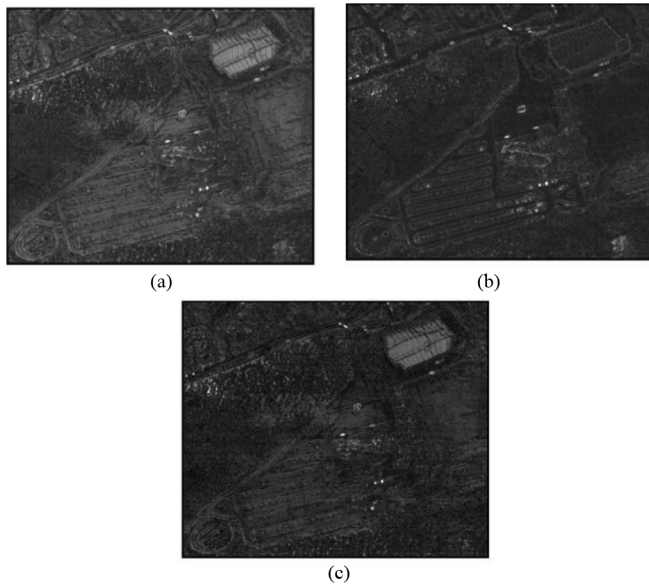
Fig. 9. ACD statistics obtained in EX-1 by means of (a) ED-ACD no RE, (b) ED-ACD-CE, and (c) ED-ACD-ELM.

Fig. 10. Ex-ROC curves obtained by applying the three considered ACD schemes to the images in EX-1.

considered image pair is displayed in Fig. 6(c). Both examples make use of de-striped and spectrally binned hyperspectral data (i.e., preprocessing level #3 in Fig. 7).

ACD is accomplished by using a detection scheme involving the well-known Euclidean distance (ED)-based algorithm (ED-ACD) [34] in conjunction with the LCRA approach [35]. Since the RMRE magnitude is not *a priori* known, it is estimated from the data themselves by resorting to the recently proposed algorithm named sequential misregistration noise estimator [7]. Three different ACD schemes are considered and compared, where 1) no RE is involved (ED-ACD no RE); 2) RE is performed by applying the CE algorithm to the at-sensor radiance data (ED-ACD-CE); 3) the analyzed images are transformed in the reflectance domain with the ELM (ED-ACD-ELM) by exploiting the ground spectral measurements included in the ground truth.

The availability of reliable CRMs including most of the small changes occurred in the monitored scenes allows the experimental-receiver operating characteristics (ex-ROC) [8] curves to be drawn for ACD algorithm performance comparison. Ex-ROC plot the fraction of detected changes or changed targets (*FoDT*) versus the FAR computed over a particular operational scenario. *FoDT* is computed as the fraction of changed targets detected with a given value of the CD threshold λ. For the same threshold λ, *FAR* is computed as the ratio between the number of pixels whose test statistic is higher than λ but that are not associated with true changes and the total number of background pixels, i.e., those not marked in the CRM.

3) ACD Experimental Results: Fig. 9 (a)–(c) shows the ACD statistics obtained in EX-1 for the three detection schemes. The statistics were scaled in the [0,1] range and gamma corrected only for visualization purposes. The ACD statistics in Fig. 9 appear very similar. Each of them assumes the highest values in correspondence of the pixels associated with the changes documented by the corresponding CRM [Fig. 6(a)]. It seems that the ED-ACD-CE provides slightly
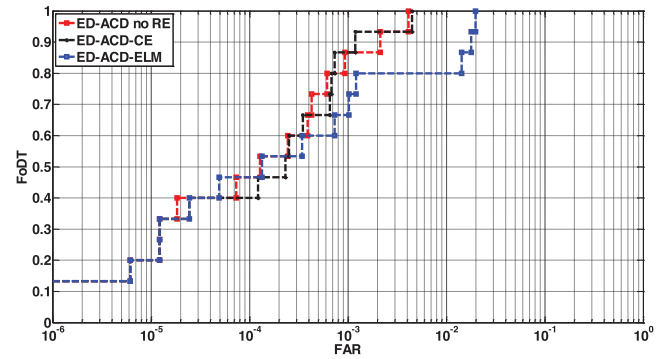
better performance in terms of background suppression. The similar behavior of the three ACD schemes is also confirmed by the ex-ROCs in Fig. 10, which exhibit very similar trends across the three curves. More specifically, on these data, ED-ACD no RE and ED-ACD-CE performed approximately the same, whereas ED-ACD-ELM provided slightly worse performance, as is evident by looking at its ex-ROC curve that deviates, with respect to the other two curves, toward higher *FAR* values for *FoDT* greater than 0.8.

The observed similarity among the three algorithms' performance is motivated by the fact that the considered ACD schemes mainly differ for the RE procedure and that the two analyzed images were acquired on the same day and with a time delay of a few minutes and, thus, without significant difference in illumination and atmospheric conditions. This makes the shared image pair adopted in EX-1 suitable for testing the steps of the ACD processing chain specifically dedicated to the pure detection of changes, without placing particular emphasis on the RE step.

The ACD statistics obtained in EX-2 are represented in Fig. 11(a)–(c). In this experiment, both the ED-ACD-CE and the ED-ACD-ELM statistics assume the highest values for those pixels corresponding to the changes documented by the CRM and lower values for most of background pixels. A similar consideration cannot be made for the ED-ACD no RE, which does not exhibit a clear distinction between the changes highlighted in the CRM and the remaining image pixels. This is due to the fact that the images considered in EX-2 were acquired in different days and with very different illumination and atmospheric conditions. Thus, contrary to EX-1, in EX-2, the RE step plays a relevant role in the ACD processing chain. This is confirmed by the ex-ROCs shown in Fig. 12. They show that, in this case, the lack of the RE step is detrimental for the overall ACD performance. In fact, the curve for ED-ACD no RE is well below those corresponding to the other two algorithms. Furthermore, Fig. 12 shows that, in this experiment, the CE is more effective than the ELM in making the two images radiometrically comparable. This could also be inferred by visual inspection of the corresponding ACD statistics in Fig. 11(b) and 11(c). By a careful analysis of these two ACD statistics, it is evident that EX-2 results also highlight the weakness common to both CE and ELM in performing the RE task when space-variant acquisition conditions affect the two analyzed
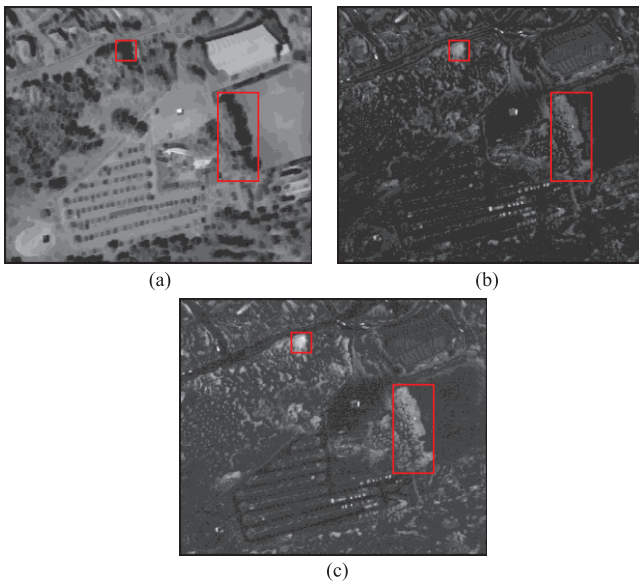
(a)   (b)

(c)

Fig. 11. ACD statistics obtained in EX-2 by means of (a) ED-ACD no RE, (b) ED-ACD-CE, and (c) ED-ACD-ELM.
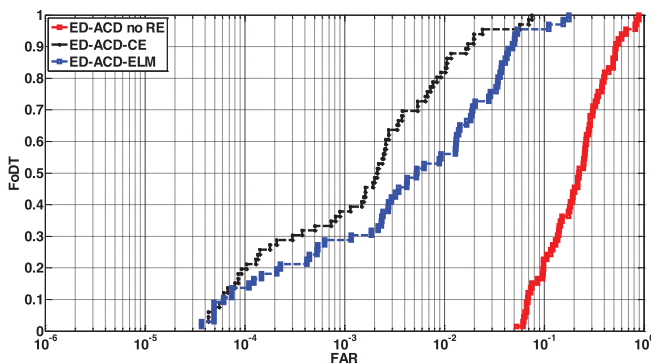

Fig. 12. Ex-ROC curves obtained by applying the three considered ACD schemes to the images in EX-2.

images. By comparing ED-ACD-CE and ED-ACD-ELM statistics with the RGB representations of "test" and "reference" images [Fig. 3(a) and 3(c)], it can be seen that high values in the ACD statistics correspond not only to true changes but also to those pixels located in shadowed areas in one of the two images. This is evident by looking at the shadowed areas enclosed in the red boxes in Fig. 11(b) and 11(c). The pixels falling in those areas have values comparable to those of the pixels containing the true changes for both algorithms.

The different acquisition conditions of the shared image pair adopted in EX-2 make this image pair suitable for testing the effectiveness of the RE algorithm involved in the ACD processing chain. Furthermore, the presence of shadowed areas in one of the images makes the data particularly useful for developing and testing RE algorithms that account for space-variant conditions in the two acquisitions [5].

V. CONCLUSION

This paper has presented a new hyperspectral data set released to the scientific community for detection algorithm

evaluation purposes. The availability of this new data contributes to improve the set of unrestricted hyperspectral imagery expressly conceived to encourage testing, comparison, and benchmarking of target detection algorithms.

The released data set currently includes three multitemporal images acquired over a suburban scenario were several different targets were deployed together with reference tarps for in-scene calibration. Various scenarios were accurately planned and set up in order to enable AD, SSBTD, and ACD experiments. Ground truth was rigorously carried out including target and calibration tarp localization and spectra collection, as well as accurate recording of movements and changes occurred in-between subsequent acquisitions. The images are released with five different levels of preprocessing. An *ad hoc* website was set up and dedicated to the distribution of data and related ground truth documentation.

A brief overview of the potential exploitation of the shared data has been presented as concerns noise estimation and reduction, AD, SSBTD, and ACD. Furthermore, an extensive example of data exploitation for ACD tasks has been provided. Experimental results featuring ACD experiments over two shared image pairs highlight the usefulness of the shared data set not only for testing and comparing the overall performance of various ACD algorithms but also for specifically focusing on each given step of the ACD processing chain, with the aim of identifying the weak links in the ACD chain and set the basis for further improvements and developments.

In the future, further images acquired during the same collection campaign over various different scenarios, ranging from beach to urban, are likely to be released, thus increasing the archive of unrestricted data set for detection algorithm comparison with data featuring different scenarios, materials, objects, and conditions.

REFERENCES

[1] Purdue Research Foundation. (1994). A freeware multispectral image data analysis system [Online]. Available: https://engineering.purdue.edu/~biehl/MultiSpec/index.html
[2] Universidad del País Vasco. (2014). Hyperspectral remote sensing scenes [Online]. Available: http://www.ehu.eus/ccwintco/index.php?title=Hyperspectral_Remote_Sensing_Scenes
[3] N. Acito, M. Diani, and G. Corsini, "Signal-dependent noise modeling and model parameter estimation in hyperspectral images," *IEEE Trans. Geosci. Remote Sens.*, vol. 49, no. 8, pp. 2957–2971, Aug. 2011.
[4] N. Acito, M. Diani, and G. Corsini, "Residual striping reduction in hyperspectral images," in *Proc. 17th Int. Conf. Digital Signal Process.*, 2011, vol. 1, pp. 1–7.

[5] N. Acito, M. Diani, A. Rossi, and S. U. de Ceglie, "Hyperspectral anomalous change detection in the presence of non-stationary atmospheric/illumination conditions," *Proc. SPIE*, vol. 9244, p. 92440Z-1-10, 2014.

[6] N. Acito, M. Diani, and G. Corsini, "On the CFAR property of the RX algorithm in the presence of signal dependent noise in hyperspectral images," *IEEE Trans. Geosci. Remote Sens.*, vol. 51, no. 6, pp. 3475–3491, Jun. 2013.

[7] N. Acito, S. Resta, M. Diani, and G. Corsini, "Residual misregistration noise estimation in hyperspectral anomalous change detection," *Opt. Eng.*, vol. 51, no. 11, p. 111705, 2012.

[8] N. Acito, S. Resta, M. Diani, and G. Corsini, "Robust technique for anomalous change detection in airborne hyperspectral imagery based on automatic and adaptive band selection," *Opt. Eng.*, vol. 52, no. 3, p. 036202, 2013.

[9] A. Berk, L. S. Bernstein, and D. C. Robertson, "MODTRAN: A moderate resolution model for LOWTRAN 7, Spectral sciences," Spectral Sci. Inc., Burlington, MA, USA, Tech Rep. GLTR890122, 1989.

[10] Y. Cohen, Y. August, D. G. Blumberg, and S. R. Rotman, "Evaluating subpixel target detection algorithms in hyperspectral imagery," *J. Electr. Comput. Eng.*, vol. 2012, pp. 103286-1–103286-14, Jun. 2012.

[11] B. Du and L. Zhang, "A discriminative metric learning based anomaly detection method," *IEEE Trans. Geosci. Remote Sens.*, vol. 52, no. 11, pp. 6844–6857, Nov. 2014.

[12] J. E. Fowler and Q. Du, "Anomaly detection and reconstruction from random projections," *IEEE Trans. Image Process.*, vol. 21, no. 1, pp. 184–195, Jan. 2012.

[13] A. Giannandrea *et al.*, "The SHARE 2012 data campaign," *Proc. SPIE*, vol. 8743, p. 87430F-1-15, 2013.

[14] T. V. Haavardsholm, T. Skauli, and I. Kasen, "A physics-based statistical signature model for hyperspectral target detection," in *Proc. IEEE Geosci. Remote Sens. Symp. (IGARSS)*, 2007, vol. 1, pp. 3198–3201.

[15] T. Haavardsholm, A. Kavara, I. Kåsen, and T. Skauli, "Improving anomaly detection with multinormal mixture models in shadow," in *Proc. IEEE Geosci. Remote Sens. Symp. (IGARSS)*, 2012, vol. 1, pp. 5478–5481.

[16] J. A. Herweg *et al.*, "Spectir hyperspectral airborne rochester experiment data collection campaign," *Proc. SPIE*, vol. 8390, pp. 554–565, 2012.

[17] W. Hongqing and C. Erle Ellis, "Image misregistration error in change measurements," *Photogramm. Eng. Remote Sens.*, vol. 71, no. 9, pp. 1037–1044, 2005.

[18] J. P. Kerekes and D. Snyder, "Unresolved target detection blind test project overview," *Proc. SPIE*, vol. 7695, pp. 1–8, Apr. 2010.

[19] H. Kwon and N. M. Nasrabadi, "Kernel RX-algorithm: A nonlinear anomaly detector for hyperspectral imagery," *IEEE Trans. Geosci. Remote Sens.*, vol. 43, no. 2, pp. 388–397, Feb. 2005.

[20] D. Manolakis, R. Lockwood, T. Cooley, and J. Jacobson, "Is there a best hyperspectral detection algorithm?," *Proc. SPIE*, vol. 7334, p. 733402-1-16, 2009.

[21] S. Matteoli, F. Carnesecchi, M. Diani, G. Corsini, and L. Chiarantini, "Comparative analysis of hyperspectral anomaly detection strategies on a new high spatial and spectral resolution data set," *Proc. SPIE*, vol. 6748, p. 67480E-1-11, 2007.

[22] S. Matteoli, M. Diani, and G. Corsini, "A tutorial overview of anomaly detection in hyperspectral images," *IEEE Aerosp. Electron. Syst. Mag. Tuts.*, vol. 25, no. 7, pp. 5–28, Jul. 2010.

[23] S. Matteoli, E. J. Ientilucci, and J. P. Kerekes, "Operation and performance considerations of radiative-transfer modeling in hyperspectral target detection," *IEEE Trans. Geosci. Remote Sens.*, vol. 49, no. 4, pp. 1343–1355, Apr. 2011.

[24] S. Matteoli, T. Veracini, M. Diani, and G. Corsini, "Models and methods for automated background density estimation in hyperspectral anomaly detection," *IEEE Trans. Geosci. Remote Sens.*, vol. 51, no. 5, pp. 2837–2852, May 2013.

[25] J. Meola, M. T. Eismann, R. L. Moses, and J. N. Ash, "Modeling and estimation of signal-dependent noise in hyperspectral imagery," *Appl. Opt.*, vol. 50, no. 21, pp. 3829–3846, 2011.

[26] S. Resta, N. Acito, M. Diani, G. Corsini, T. Opsahl, and T. Haavardsholm, "Detection of small changes in airborne hyperspectral imagery: Experimental results over urban areas," in *Proc. 6th Int. Workshop Anal. Multi-Temp. Remote Sens. Images (Multi-Temp)*, 2011, pp. 5–8.

[27] A. Rossi *et al.*, "Hyperspectral data collection for the assessment of target detection algorithms: The Viareggio 2013 trial," *Proc. SPIE*, vol. 9250, p. 92500V-1-14, 2014.

[28] A. Schaum and A. Stocker, "Hyperspectral change detection and supervised matched filtering based on covariance equalization," *Proc. SPIE*, vol. 5425, pp. 77–90, 2004.

[29] A. Schaum and A. Stocker, "Linear chromodynamics models for hyperspectral target detection," in *Proc. IEEE Aerosp. Conf.*, 2003, vol. 4, pp. 1879–1885.

[30] A. Schaum and A. Stocker, "Long-interval Chronochrome target detection," in *Proc. Int. Symp. Spectral Sens. Res.*, 1998.

[31] J. R. Schott, *Remote Sensing: The Image Processing Chain*. London, U.K.: Oxford Univ. Press, 2007.

[32] D. Snyder, J. Kerekes, I. Fairweather, R. Crabtree, J. Shive, and S. Hager, "Development of a web-based application to evaluate target finding algorithms," in *Proc. IEEE Geosci. Remote Sens. Symp. (IGARSS)*, 2008, vol. 2, pp. 915–918.

[33] B. Thai and G. Healey, "Invariant subpixel detection in hyperspectral imagery," *IEEE Trans. Geosci. Remote Sens.*, vol. 40, no. 3, pp. 599–608, Mar. 2002.

[34] J. Theiler, "Quantitative comparison of quadratic covariance-based anomalous change detectors," *Appl. Opt.*, vol. 47, pp. F12–F26, 2008.

[35] J. Theiler and B. Wohlberg, "Local coregistration adjustment for anomalous change detection," *IEEE Trans. Geosci. Remote Sens.*, vol. 50, no. 8, pp. 3107–3116, Aug. 2012.

[36] M. L. Uss, B. Vozel, V. V. Lukin, and K. Chehdi, "Local signal-dependent noise variance estimation from hyperspectral textural images," *IEEE J. Sel. Topics Signal Process.*, vol. 5, no. 3, pp. 459–486, Jun. 2011.

[37] E. J. Kelly, "An adaptive detection algorithm," *IEEE Trans. Aerosp. Electron. Syst.*, vol. AES-22 no. 2, pp. 115–127, Mar. 1986.

[38] S. Kraut and L. L. Scharf, "The CFAR adaptive subspace detector is a scale-invariant GLRT," *IEEE Trans. Signal Process.*, vol. 47 no. 9, pp. 2538–2541, Sep. 1999.

[39] J. M. Bioucas-Dias and J. M. P. Nascimento, "Hyperspectral Subspace Identification," *IEEE Trans. Geosci. Remote Sens.*, vol. 46, no. 8, pp. 2435–2445, Aug. 2008.

Nicola Acito (M'02) received the Laurea degree (*cum laude*) in telecommunication engineering and the Ph.D. degree in "methods and technologies for environmental monitoring" from the University of Pisa, Pisa, Italy, in 2001 and 2005, respectively.

From November 2004 to October 2008, he was a Temporary Researcher with the Department of Information Engineering, University of Pisa. He is currently a Researcher/Lecturer with the Italian Navy Academy, Livorno, Italy. His research interests include signal and image processing in remote sensing applications, and target detection and recognition in hyperspectral images.

Dr. Acito is a Reviewer of the most important international journals, i.e., the IEEE TRANSACTIONS ON GEOSCIENCE AND REMOTE SENSING, the IEEE TRANSACTIONS ON SIGNAL PROCESSING, the IEEE TRANSACTIONS ON IMAGE PROCESSING, and the IEEE TRANSACTIONS ON AEROSPACE AND ELECTRONIC SYSTEMS.

Stefania Matteoli (S'06–M'11) received the B.S. and M.S. (*cum laude*) degrees in telecommunications engineering and the Ph.D. degree in remote sensing from the University of Pisa, Pisa, Italy, in 2003, 2006, and 2010 respectively.

She is currently a Researcher with the Department of Information Engineering, University of Pisa, where she has been teaching laboratory classes of "design and simulation of remote sensing systems" and "environmental monitoring systems." From May 2008 to October 2008, she was a Visiting Student at the Chester F. Carlson Center for Imaging Science, Rochester Institute of Technology, Rochester, NY, USA. Her research interests include signal and image processing, anomaly and object detection methodologies for multihyperspectral remotely sensed images, radiation transfer modeling for spectral signature based object detection in hyperspectral images, fluorescence LIDAR signal processing for underwater object detection and recognition, and nondestructive spectroscopy-based methodology for fruit quality monitoring.

Dr. Matteoli has served as a Reviewer for journals such as the IEEE TRANSACTIONS ON GEOSCIENCE AND REMOTE SENSING, the IEEE GEOSCIENCE AND REMOTE SENSING LETTERS, the IEEE JOURNAL OF SELECTED TOPICS IN APPLIED EARTH OBSERVATION AND REMOTE SENSING, the *Journal of Applied Remote Sensing*, the IEEE TRANSACTIONS ON PATTERN ANALYSIS AND MACHINE INTELLIGENCE, the IEEE TRANSACTIONS ON SYSTEMS, MAN, AND CYBERNETICS, and *Infrared Physics and Technology*.

Alessandro Rossi received the B.S. and M.S. degrees in telecommunications engineering and the Ph.D. degree in remote sensing from the University of Pisa, Pisa, Italy, in 2005, 2008, and 2012, respectively.

He is currently an Altran Consultant Engineer with the Imagers Department, FINMECCANICA, Florence, Italy. His research interests include hyperspectral data exploitation, with focus on design of real-time processing algorithms.

Marco Diani (M'93) received the Laurea degree (*cum laude*) in electronic engineering from the University of Pisa, Pisa, Italy, in 1988.

He is currently a Full Professor with the Italian Naval Academy, Livorno, Italy, where he teaches "signal processing" and "telecommunications theory." He also teaches "remote sensing" at the University of Pisa. His research interests include image and signal processing with application to remote sensing. In this framework, his works have covered different topics such as data fusion, signal processing in imaging radars, image classification and segmentation, and object detection. His recent activities have focused on the development of new algorithms for object detection and tracking in infrared image sequences and on target detection and recognition in multi/hyperspectral images.

Prof. Diani is Associate Editor for the *Journal of Applied Remote Sensing* (JARS) and for the *Journal of Real Time Image Processing* (JRTIP). He has served as a Reviewer for many journals in the fields of remote sensing and image/signal processing such as the IEEE Transactions on Image Processing, the IEEE Transactions on Signal Processing, the IEEE Transactions on Geoscience and Remote Sensing, *Applied Optics*. He is member of SPIE.

Giovanni Corsini (M'89) received the Laurea degree in electronic engineering from the University of Pisa, Pisa, Italy, in 1979.

He is currently a Full Professor with the Department of Information Engineering, University of Pisa, where he teaches "image processing." His research interests include signal detection and processing with emphasis on image and multidimensional signal analysis in remote sensing applications, and object detection and parameter estimation from remotely sensed data with particular emphasis on hyperspectral and multispectral images.

Prof. Corsini has been a member of technical committees at international conferences. He is a Reviewer of the most important international journals in this field, i.e., the IEEE Transactions on Geoscience and Remote Sensing, the IEEE Transactions on Image Processing, the IEEE Transactions on Signal Processing, the IEEE Transactions on Aerospace and Electronic Systems, and the *International Journal on Remote Sensing*.